INTERNATIONAL JOURNAL FOR NUMERICAL METHODS IN FLUIDS, VOL. 22, 581–601 (1996)

A PRESSURE-CORRECTION METHOD FOR THE SOLUTION OF INCOMPRESSIBLE VISCOUS FLOWS ON UNSTRUCTURED GRIDS

MICHAEL THOMADAKIS AND MICHAEL LESCHZINER

Department of Mechanical Engineering, UMIST, PO Box 88, Manchester M60 1QD, U.K.

SUMMARY

An unstructured grid, finite volume method is presented for the solution of two-dimensional viscous, incompressible flow. The method is based on the pressure-correction concept implemented on a semi-staggered grid. The computational procedure can handle cells of arbitrary shape, although solutions presented herein have been obtained only with meshes of triangular and quadrilateral cells. The discretization of the momentum equations is effected on dual cells surrounding the vertices of primary cells, while the pressure-correction equation applies to the primary-cell centroids and represents the conservation of mass across the primary cells. A special interpolation scheme s used to suppress pressure and velocity oscillations in cases where the semi-staggered arrangement does not ensure a sufficiently strong coupling between pressure and velocity to avoid such oscillations. Computational results presented for several viscous flows are shown to be in good agreement with analytical and experimental data reported in the open literature.

KEY WORDS: unstructured grids; incompressible viscous flow; pressure-correction method

1. INTRODUCTION

Unstructured grid schemes are increasingly held to form the basis of future CFD technology in all areas of engineering applications. While posing not inconsiderable challenges in the context of turbulent near-wall flow, unstructured grids are steadily gaining in popularity, especially in CFD for aeronautical and aerospace applications, for they offer exceptional geometric flexibility and permit virtually unrestricted local grid-density control and flow-sensitized, dynamic adaptation.

Although the methodology is rooted in the finite element environment, it may be readily implemented within the finite volume framework, the principal advantages being the unconditional satisfaction of the conservation principle inherent in the flow-governing transport equations and the relative simplicity of the approximation process. Both advantages arise from the fact that the discretization simply involves the application of a volume integral of any transport equation over the cells formed by the unstructured grid, which can then be expressed as a balance of cell-face fluxes.

Because of the special significance of unstructured grids to the complex geometries encountered in external aerodynamics and the relative simplicity of the flow physics involved in this environment, efforts made over the past few years have focused principally on compressible flow in which the conservation laws governing mass and momentum are solved with a time-marching scheme to yield the density and velocity fields. For *incompressible* conditions this is at best inefficient and at worst

CCC 0271–2091/96/0705871–21

Received April 1995
Revised June 1995

unstable. Indeed, it is only tenable in conjunction with an artificial compressibility linking density to pressure via a fictitious relationship—an approach which can only be used if a steady-state solution is sought. The widely used alternative in the structured-grid environment is the solution of the pressure or pressure-correction equation, which replaces that describing mass continuity. The implementation of this technique within the unstructured-grid environment is relatively recent.

Early work on incompressible flow has progressed within the finite element framework or variants thereof. Patankar and his associates,[1–4] Prakash,[5,6] Prakash and Pataknar[7,8] and Baliga and his group[9–12] have introduced and implemented the concept of the control volume finite element method (CVFEM). Alternative storage arrangements for pressure and velocity were adopted and investigated in conjunction with either unequal-order interpolation functions or with uniform-order interpolation for collocated pressure and velocities. The approximation of the convective face fluxes was based on exponential differencing, and the pressure was determined by means of the SIMPLER or SIMPLEC algorithms which are standard practices in the structured-grid environment.

Much more recent is the formulation of unstructured-grid, *finite volume* schemes for incompressible flow. Lonsdale and Webster[13] have proposed a pressure-correction approach on a grid consisting of hexahedra. Despotis and Tsangaris[14] have introduced a modified Chorin method[15] for unstructured staggered grids. Williams[16] has presented a segregated, collocated, cell-vertex Helmholz pressure scheme. Watterson[17] has adopted a cell vertex, collocated, Runge–Kutta time-marching scheme to integrate the decoupled system of momentum and pressure-correction equations in time. The last two schemes involved the use of explicit artificial dissipation to remove pressure oscillations arising from pressure–velocity decoupling, which is a consequence of the collocated storage arrangement. On the other hand, Gosman *et al.*[18] and Raw *et al.*[19] have adopted a form of the interpolation practice originally proposed by Rhie and Chow[20] for collocated, structured-grid schemes. This practice counteracts chequerboard oscillations by introducing implicitly a stabilizing fourth-order diffusion term. The last two methods have been developed for quadrilateral cells in 2D space and hexahedral cells in the 3D environment, both offering a node arrangement analogous to that present in a structured grid and thus easing the adaptation of the Rhie–Chow interpolation technique.

This paper presents a new variant of the unstructured finite volume method formulated for the solution of 2D steady, viscous, incompressible flows. The scheme employs arbitrarily shaped, semi-staggered control volumes for the momentum and pressure-correction equations to promote pressure–velocity coupling, but a single set of nodes (the vertices of the primary cells) is used to store the Cartesian velocity components. The data structure is constructed in such a way that the cells of the unstructured grid can be polygons of any shape and number of edges. However, as unstructured meshes with cell shapes other than triangles and quadrilaterals are neither useful nor easily generated, results are presented only for meshes consisting of cells of these two shapes. Although the semi-staggered formulation provides, in the majority of applications, adequate damping of pressure–velocity oscillations, it is occasionally necessary to introduce a small measure of additional dissipation. To this end, the above-mentioned Rhie–Chow scheme is adapted for use in the unstructured-grid environment and applied to cell-face velocities which contribute to the mass imbalance term of the pressure-correction equation.

2. GOVERNING EQUATIONS

Within the finite volume framework, the most appropriate basis for the discretization process is the integral form of the conservation laws. When a set of non-overlapping volumes is used to cover the computational domain, this form of equations guarantees local and global conservation provided that the discretized equations are satisfied (i.e. once the numerical solution algorithm has yielded a fully converged state).

In this study, attention is confined to steady, laminar, incompressible 2D flows, in which case the integral forms of the continuity and momentum equations can be written, respectively, as

$$\int_E \vec{c}\vec{n}\,\mathrm{d}E = 0 \tag{1}$$

$$\int_E u\vec{c}\vec{n}\,\mathrm{d}E = -\int_E pn_x\,\mathrm{d}E + \frac{1}{Re}\int_E (\tau_{xx}n_x + \tau_{xy}n_y)\,\mathrm{d}E, \tag{2}$$

$$\int_E v\vec{c}\vec{n}\,\mathrm{d}E = -\int_E pn_y\,\mathrm{d}E + \frac{1}{Re}\int_E (\tau_{xy}n_x + \tau_{yy}n_y)\,\mathrm{d}E. \tag{3}$$

In writing the above equations, the following assumptions have been made.

(a) All variables are in non-dimensional form.

(b) The density and viscosity of the fluid are invariant and equal to their respective reference values used for normalization.

(c) The Reynolds number Re is given by

$$Re = U_{\mathrm{ref}}L_{\mathrm{ref}}/\nu_{\mathrm{ref}}. \tag{4}$$

(d) E is the closed surface surrounding the control volume over which the conservation of mass and momentum is considered; $\vec{n}$ is the unit vector normal to E, positive when directed outwards, with n_x and n_y its components along the Cartesian axes x and y respectively.

(e) $\vec{c} = u\vec{i} + v\vec{j}$ is the velocity vector, with u and v its components along the Cartesian axes x and y respectively.

(f) τ_{xx}, τ_{xy}, etc. are the components of the shear stress tensor.

3. APPROXIMATION

3.1. The generic cell

The control volume over which equation (1) is to be applied is a polygon which consists of an arbitrary number of straight edges. Using the notation in Figure 1, the unit vector can be written as

$$\vec{n}\,\mathrm{d}E = \Delta y\vec{i} - \Delta x\vec{j}, \tag{5}$$

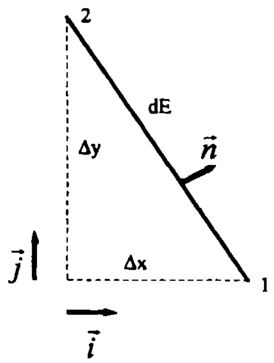

Figure 1. Notation associated with equations (1)–(3) and (5)

where $\Delta x = x_2 - x_1$ and $\Delta y = y_2 - y_1$. This notation is consistent with an integration of any conservation equation over the control volume in counterclockwise direction.

The approximation of the contour integrals in the governing equations (1)–(3) is effected by a summation of fluxes over the edges of the numerical polygonal control volume and use of equation (5) for the normal unit vector. This process results in the following discretized form of the governing equations:

$$\sum_{i=1}^{ie} [(u\Delta y)_e - (v\Delta x)_e] = 0, \tag{6}$$

$$\sum_{i=1}^{ie} u_e[(u\Delta y)_e - (v\Delta x)_e] = -\sum_{i=1}^{ie} p_e\Delta y_e + \frac{1}{Re}\left(\sum_{i=1}^{ie}(\tau_{xx})_e\Delta y_e - \sum_{i=1}^{ie}(\tau_{xy})_e\Delta x_e\right), \tag{7}$$

$$\sum_{i=1}^{ie} v_e[(u\Delta y)_e - (v\Delta x)_e] = \sum_{i=1}^{ie} p_e\Delta x_e + \frac{1}{Re}\left(\sum_{i=1}^{ie}(\tau_{xy})_e\Delta y_e - \sum_{i=1}^{ie}(\tau_{yy})_e\Delta x_e\right), \tag{8}$$

where the subscript e denotes a quantity on any edge and ie is the total number of edges that form the closed numerical control volume.

3.2. Pressure–velocity coupling

There are three major approaches to the solution of the system of equations *(6)–(8) for incompressible* flow: the first is the pseudocompressibility approach;[15] the second is based on the coupled block-implicit solution of the momentum and continuity equations;[21] the third is the decoupled solution for the velocity and pressure fields, the last involving a replacement of the continuity equation by an analogous equation from which the pressure can be determined. There are two common alternative options within the last route: transforming the continuity equation into a Poisson equation for the pressure or replacing this equation by an approximate equivalent for the pressure correction. In the present study the latter option has been chosen.

A central issue in the solution of the system of governing equations within a pressure-based scheme is the manner in which the natural coupling between the velocity and pressure fields is maintained numerically. Here, strong coupling is secured by using a staggered storage wherein velocities are defined at vertices of the primary cells while pressure is defined at cell centres (Figure 2). Following the SIMPLE approach of Patankar and Spalding,[22] the velocity and pressure fields are considered to each consist of a *provisional part* and a *correction*:

$$p = p^* + p', \qquad u = u^* + u', \qquad v = v^* + v', \tag{9}$$

where the asterisk denotes the provisional part and the prime the correction.

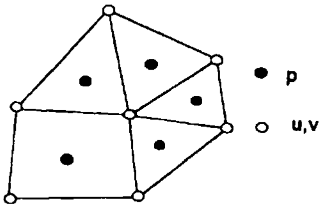

Figure 2. Present storage arrangement

3.3 Momentum equations

In order to derive the discrete form of the momentum equations (7) and (8), a numerical control volume must be defined over which the numerical integration can be performed. In the present staggered approach, where a cell-vertex storage arrangement is followed for the velocities, the most appropriate choice for this volume is the *centroid dual* of the primary cells. This polygon is formed by connecting the centres of the cells which meet at the same vertex. Figure 3 depicts one such polygon around the central vertex iv_2 for both triangular and quadrilateral meshes. In what follows, this polygon will be referred to as the *macrovolume*.

The discretization procedure entails the evaluation of the various terms in equations (7) and (8) on the edges of the macrovolume. With attention focused on the edge ic_1–ic_2 (Figure 3), the approximation adopted for the convective terms, diffusive fluxes and pressure on this edge are given below for the x-momentum equation.

Convective terms. These are given by

$$convection_{ic_1-ic_2} = u_{ic_1-ic_2} flux_{ic_1-ic_2}, \tag{10}$$

$$flux_{ic_1-ic_2} = (\vec{c}\cdot\vec{n})_{ic_1-ic_2} = (u\Delta y)_{ic_1-ic_2} - (v\Delta x)_{ic_1-ic_2}. \tag{11}$$

Since no temporal fragment exists here, the above terms provide the most important contributions to the diagonal coefficient of the final linear system of equations governing the velocity components. If, for the sake of enhanced stability, a first-order upwind scheme is used to approximate $u_{ic_1-ic_2}$ in equation (10), i.e.

$$u|_{ic_1-ic_2} flux_{ic_1-ic_2} = k_1 u_{iv_2} - k_2 u_{iv_1}, \tag{12}$$

$$k_1 = \max(0, flux_{ic_1-ic_2}), \qquad k_2 = \max(0, -flux_{ic_1-ic_2}), \tag{13}$$

then the components of the fluxes on the edge arise as

$$(u\Delta y)_{ic_1-ic_2} = \tfrac{1}{2}(u_{ic_1} + u_{ic_2})(y_{ic_1} - y_{ic_2}), \qquad (v\Delta x)_{ic_1-ic_2} = \tfrac{1}{2}(v_{ic_1} + v_{ic_2})(x_{ic_1} - x_{ic_2}). \tag{14}$$

The velocities at the cell centres that are involved in equation (14) are obtained by a distance-weighted interpolation from surrounding cell-vertex values.

Diffusive terms. The viscous terms that appear in equation (7) require the approximation of velocity derivatives on the edges of the centroid dual. To this end, the auxiliary control volume shown in Figure

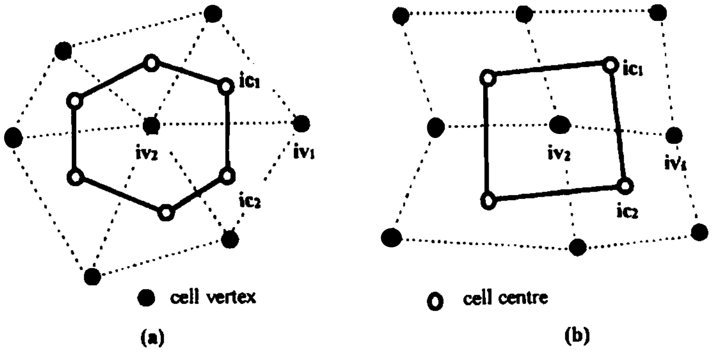

Figure 3. Control volumes for momentum equations: (a) triangular mesh; (b) quadrilateral mesh

4 is used. Velocity derivatives are considered invariant within this control volume and are approximated by the expression

$$\frac{\partial u^i}{\partial x^j} = \frac{(-1)^{j+1}}{2V_e} \sum_{k=1}^{4} u_k^i (x_{k+1}^{j+1} - x_{k-1}^{j+1}), \tag{15}$$

where $i = 1, 2$ (cyclic), $j = 1, 2$ (cyclic), $k = 1, \dots, 4$ (cyclic), $u^1 = u$, $u^2 = v$, $x^1 = x$, $x^2 = y$ and V_e is the area of the auxiliary control volume.

Pressure. The average pressure along any edge of the macrovolume cell is approximated by means of the trapezoidal rule using pressures stored at appropriate centroids of the primary cells. Thus, for the edge ic_1–ic_2 of Figure 3,

$$p_{ic_1-ic_2} = \tfrac{1}{2}(p_{ic_1} + p_{ic_2}). \tag{16}$$

Final momentum equations. Insertion of equations (12)–(16) into the x-momentum equation (7) yields an expression that relates the velocity value at the central vertex of Figure 3 to the velocities and pressures at neighbouring vertices. If, in addition, the pressure and velocity values in this expression are replaced by the corresponding provisional values in the sense of equation (9), then the final equation for the provisional velocity u^* at the vertex iv_2 becomes

$$A^u_{iv_2} u^*_{iv_2} = -\tfrac{1}{2} \sum_{i=1}^{ie} (p^*_i + p^*_{i+1})(y^c_{i+1} - y^c_i) + \sum_{i=1}^{ie} A^u_i u^*_{v_i} + \sum_{j=1}^{nb} A^u_{nb} C^u_{nb}(u, v). \tag{17}$$

Equation (17) is the final discretized form of the x-momentum equation. The first term on the right-hand side contains the pressure at the vertices of the macrovolume (cell centres of the primary cells), the second contains the provisional velocities at the vertices of the cells that meet at iv_2, and the third contains all the velocity fragments which cannot be incorporated into the diagonal (left-hand-side) term or the second term on the right-hand side. This last term contains u- and v-velocity fragments residing at the cell centres surrounding iv_2. In the solution sequence, the values of these velocity terms are set equal to their values in the previous global iteration.

The corresponding discretized form of the y-momentum equation arises as

$$A^v_{iv_2} v^*_{iv_2} = \tfrac{1}{2} \sum_{i=1}^{ie} (p^*_i + p^*_{i+1})(x^c_{i+1} - x^c_i) + \sum_{i=1}^{ie} A^v_i v^*_{v_i} + \sum_{j=1}^{nb} A^v_{nb} C^v_{nb}(u, v). \tag{18}$$

Equations (17) and (18), when written for all the vertices, give the two linear systems of equations which yield values for the provisional velocity components provided that the pressure field is known. Here, the solution of these two systems is performed by a segregated point Gauss–Seidel procedure. For each vertex, a loop over the edges that form the centroid dual around that vertex is performed to evaluate the various terms in equations (6) and (7), and then the velocity on that edge is computed. In

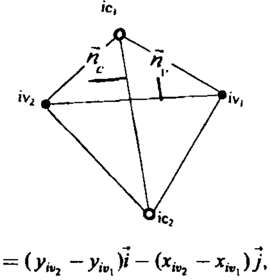

Figure 4. Auxiliary control volume $\vec{n}_v = (y_{iv_2} - y_{iv_1})\vec{i} - (x_{iv_2} - x_{iv_1})\vec{j}$, $\vec{n}_c = (y_{ic_2} - y_{iv_1})\vec{i} - (x_{ic_2} - x_{ic_1})\vec{j}$

most cases one or two Gauss–Seidel iterations per global iteration (consisting of a complete update for velocities and pressure) have been found to be sufficient, although this number depends on the initial pressure and velocity fields.

It is appropriate to note here that no underrelaxation has been used during the iterative Gauss–Seidel procedure for the momentum equations. Velocities have been underrelaxed only at the end of the procedure, through

$$u^*_{iv_2} = \alpha u^*_{iv_2} + (1-\alpha)u^o_{iv_2}, \qquad v^*_{iv_2} = \alpha v^*_{iv_2} + (1-\alpha)v^o_{iv_2}, \tag{19}$$

where the superscript o denotes values at the previous global iteration and α is the underrelaxation factor.

3.4. *Pressure-correction equation*

The pressure-correction equation is derived from the continuity equation integrated over the primary cells of the grid. In Figure 5 the bold lines identify the numerical control volumes for the pressure correction equation for one of the cells whose centres define the macrovolume of Figure 4. The task is to derive an equation for the pressure correction at the centre of the cell ic_2. The sole purpose of this equation is to steer the pressure to a state compatible with the mass-continuity principle.

Integration of the continuity equation (6) over this control volume and use of equation (9) gives the result

$$\sum_{i=1}^{nec}(u'_e\Delta y_e - v'_e\Delta x_e) = -\sum_{i=1}^{nec}(u^*_e\Delta y_e - v^*_e\Delta x_e) = -\sum \dot{m}^*, \tag{20}$$

where the mass-imbalance term on the right-hand side requires special treatment and will be discussed in the next section, while *nec* is the number of edges which form each primary cell.

A key issue in the discretization of equation (20) is the manner in which edge values of the velocity corrections are to be related to pressure-correction values at the adjacent cell centres. In an earlier variant of the present method[23] the discretized momentum equations (17) and (18) were linearized and truncated, in accord with the conventional SIMPLE approach, to yield linear relations linking velocity and pressure corrections at cell vertices. For example, for the vertex iv_2 of Figures 4 and 5 this practice gave

$$u'_{iv_2} = -\frac{\alpha}{2A^u_{iv_2}}\sum_{i=1}^{ie}(p'_i + p'_{i+1})(y^c_{i+1} - y^c_i), \tag{21}$$

$$v'_{iv_2} = \frac{\alpha}{2A^v_{iv_2}}\sum_{i=1}^{ie}(p'_i + p'_{i+1})(x^c_{i+1} - x^c_i), \tag{22}$$

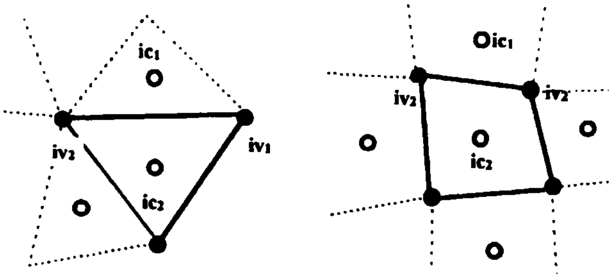

Figure 5. Control volumes for pressure correction equation

where equations (19) have also been taken into account. The edge value of the velocity correction was then related to the respective vertex values by

$$u'_{e_{iv_1-iv_2}} = \tfrac{1}{2}(u'_{iv_1} + u'_{iv_2}), \tag{23}$$

with similar expressions applicable to the v-velocity components. Combinations of equations (20)–(23) then yielded the pressure correction at the cell centre ic_2 as

$$p'_{ic_2} = \frac{1}{L_{\text{cent}}}\left(2\frac{\sum \dot{m}^*}{\alpha} - L_{\text{rest}}\right), \tag{24}$$

in which the various terms on the right-hand side arise as a natural consequence of the algebraic manipulations and are given by the expressions

$$L_{\text{cent}} = \sum_{j=1}^{nec}\left(\frac{1}{A^u_{iv_j}}[(y^v_{j+1} - y^v_{j-1})(y^{ic_2}_{k+1} - y^{ic_2}_{k-1})] + \frac{1}{A^v_{iv_j}}[(x^v_{j+1} - x^v_{j-1})(x^{ic_2}_{k+1} - x^{ic_2}_{k-1})]\right), \tag{25}$$

$$L_{\text{rest}} = \sum_{j=1}^{nec}\left[\frac{1}{A^u_{iv_j}}\left((y^v_{j+1} - y^v_{j-1})\sum_{k=1}^{ie(iv_j)_{\text{rest}}} p'_k(y^c_{k+1} - y^c_{k-1})\right) + \frac{1}{A^v_{iv_j}}\left((x^v_{j+1} - x^v_{j-1})\sum_{k=1}^{ie(iv_j)_{\text{rest}}} p'_k(x^c_{k+1} - x^c_{k-1})\right)\right]. \tag{26}$$

In equations (25) and (26), $A^{u,v}_{iv_j}$ are the diagonal coefficients of the momentum equations, iv_j ($j = 1, \ldots, nec$) are the vertices which form the primary cell, nec is the number of vertices (or edges) which form the primary cell, the superscript v denotes co-ordinates of the vertices, the superscript c denotes co-ordinates of the cell centres, ic_2 denoting the co-ordinates of the centre of the cell in question, and the notation 'rest' indicates that the cell considered (namely ic_2) must be excluded from the summation.

Unfortunately, diagonal dominance of equation (24) is not secured with the procedure described so far. This is because the coefficients a_{nb} in

$$a_P = \sum a_{nb} \tag{27}$$

are not all positive, so that the condition for diagonal dominance of the system,

$$|a_P| \geqslant \sum |\alpha_{v\beta}|, \tag{28}$$

is not satisfied, the practical manifestation being numerical instability in a number of applications.

In view of the difficulties encountered with the above method, an alternative route to deriving the pressure-correction equation was adopted. Central to this alternative approach is the assumption that the pressure gradient at each vertex can be considered equal to the mean value of the gradient over the macrovolume around the vertex. Application of the Gauss divergence theorem and use of the trapezoidal rule along each side of the macrovolume around the vertex iv_2 (Figure 3) yields the following expressions for the pressure derivatives at iv_2:

$$\begin{aligned} \left(\frac{\partial p}{\partial x}\right)_{iv_2} &= \left(\overline{\frac{\partial p}{\partial x}}\right)_{\Omega_{iv_2}} = \frac{1}{2\Omega_{iv_2}}\sum_{i=1}^{ie}(p_i + p_{i+1})(y^c_{i+1} - y^c_i), \\ \left(\frac{\partial p}{\partial y}\right)_{iv_2} &= \left(\overline{\frac{\partial p}{\partial y}}\right)_{\Omega_{iv_2}} = -\frac{1}{2\Omega_{iv_2}}\sum_{i=1}^{ie}(p_i + p_{i+1})(x^c_{i+1} - x^c_i), \end{aligned} \tag{29}$$

where Ω_{iv_2} is the area of the macrovolume around the vertex iv_2.

Combining equations (21), (22) and (29) leads to the following relationships between the velocity corrections and the derivatives of the pressure correction at iv_2:

$$u'_{iv_2} = -\frac{\alpha\Omega_{iv_2}}{A^u_{iv_2}}\left(\frac{\partial p'}{\partial x}\right)_{iv_2}, \qquad v'_{iv_2} = -\frac{\alpha\Omega_{iv_2}}{A^v_{iv_2}}\left(\frac{\partial p'}{\partial y}\right)_{iv_2}. \tag{30}$$

It is next assumed that relations of the form (30) also pertain to any edge (say e) of the primary cell over which continuity is to be satisfied:

$$u'_e = -\frac{\alpha\Omega_e}{A^u_e}\overline{\left(\frac{\partial p'}{\partial x}\right)}_e, \qquad v'_e = -\frac{\alpha\Omega_e}{A^v_e}\overline{\left(\frac{\partial p'}{\partial y}\right)}_e. \tag{31}$$

In order to obtain expressions for the pressure-correction derivatives in equation (31), the auxiliary cell shown in Figure 4 is used again. The Gauss divergence theorem for the derivatives and the trapezoidal rule for the edge values are used again to give the following expressions for the pressure derivatives within the auxiliary control volume:

$$\begin{aligned} \overline{\left(\frac{\partial p'}{\partial x}\right)}_e &= \frac{1}{2V_e}[(p'_{ic_1} - p'_{ic_2})(y_{iv_2} - y_{iv_1}) + (p'_{iv_1} - p'_{iv_2})(y_{ic_1} - y_{ic_2})], \\ \overline{\left(\frac{\partial p'}{\partial y}\right)}_e &= -\frac{1}{2V_e}[(p'_{ic_1} - p'_{ic_2})(x_{iv_2} - x_{iv_1}) + (p'_{iv_1} - p'_{iv_2})(x_{ic_1} - x_{ic_2})]. \end{aligned} \tag{32}$$

When these expressions are inserted into equations (31) and the results for the edge-velocity corrections are substituted into the continuity equation (20), the pressure correction equation for p'_{ic_2} is obtained as

$$L_{ic_2}p'_{ic_2} = -\sum \dot{m}^* + \sum_{i=1}^{nec} L_i p'_{ic_i} + \sum_{i=1}^{nec}\left[\frac{\alpha D^u_e \Delta y_i \Delta y^c_i}{2V_e} + \frac{\alpha D^v_e \Delta x_i \Delta x^c_i}{2V_e}\right](p'_{iv_1} - p'_{iv_2})_i \tag{33}$$

with

$$L_{ic_2} = \sum_{i=1}^{nec} L_i, \tag{34}$$

$$L_i = \frac{\alpha\Omega_{e_i}\Delta y_i^2}{2V_{e_i}A^u_{e_i}} + \frac{\alpha\Omega_{e_i}\Delta x_i^2}{2V_{e_i}A^v_{e_i}} = \frac{\alpha}{2V_{e_i}}(D^u_{e_i}\Delta y_i^2 + D^v_{e_i}\Delta x_i^2), \tag{35}$$

$$D^u_{e_i} = \frac{\Omega_{e_i}}{A^u_{e_i}}, \qquad D^v_{e_i} = \frac{\Omega_{e_i}}{A^v_{e_i}}. \tag{36a}$$

The terms in (36a) which pertain to the edge e are evaluated by linear interpolation from the corresponding terms at the vertices of the edge. For example, for the edge iv_1–iv_2 of Figure 5,

$$D^u_{iv_1-iv_2} = \frac{1}{2}\left(\frac{\Omega_{iv_1}}{A^u_{iv_1}} + \frac{\Omega_{iv_2}}{A^u_{iv_2}}\right), \qquad D^v_{iv_1-iv_2} = \frac{1}{2}\left(\frac{\Omega_{iv_1}}{A^v_{iv_1}} + \frac{\Omega_{iv_2}}{A^v_{iv_2}}\right). \tag{36b}$$

As should be evident from equations (34)–(36), the coefficients of the pressure corrections in equation (33) are always positive, and the condition expressed in equation (28) is therefore satisfied provided that the pressure-correction values at the vertices of the grid contained in the right-hand-side sum of equation (33) are not expressed in terms of the unknown pressure-correction values at the primary-cell centres. This independence can be achieved, for example, by setting the term to zero, which is entirely permissible, since the only purpose of the pressure-correction equation is to ensure that the mass imbalance is driven to zero. With this simplification adopted, the final form of the pressure-correction equation is given by

$$L_{ic_2}p'_{ic_2} = -\sum \dot{m}^* + \sum_{i=1}^{nec} L_i p'_{ic_i}. \tag{37}$$

The main advantage of equation (37) over (24) is that it ensures the diagonal dominance of the linear system. An added bonus is the reduced numerical stencil associated with equation (37) relative to that of (24). Both numerical stencils are presented in Figure 6 for the particular example of a triangular cell system. It will be noted that equation (37) requires, in the case of a triangular mesh, only three cells adjacent to the central cell with which the equation is associated. For a quadrilateral cell arrangement, four neighbour cells are involved.

Equation (37), when written for all the internal primary cells of the grid, gives the linear system which yields the values of the pressure correction at the cells centres. This system is solved by the same Gauss–Seidel scheme as that applied to the momentum equations. However, since all pressure-correction values are set equal to zero prior to any global iteration cycle, more internal pressure-correction sweeps than momentum iterations need to be performed per global iteration, typical sweep numbers being three to five. It has been observed that the iterative stability of the scheme as a whole is highly sensitive to details of the pressure-correction solution. In particular, when the iterative sequence commences with a velocity field which generates large mass residuals, extreme levels of pressure correction are generated and this often leads to instability. In such circumstances, the introduction of underrelaxation into the Gauss–Seidel solution for the pressure-correction equation has been found to be helpful. In the majority of the test calculations that will be presented below, no underrelaxation has been used for linear iterations or sweeps. In a few cases, an underrelaxation factor of 0·5–0·8 was used in the initial phase of the iteration process, with the value gradually increased to unity.

3.5. *The mass residual*

It is recalled that the mass residual is given by equation (20):

$$\sum \dot{m}^* = \sum_{i=1}^{nec} (u_e^* \Delta y_e - v_e^* \Delta x_e). \tag{38}$$

The task is to compute this term for each primary cell of the grid in order to form the right-hand side of the pressure-correction equation.

In a structured-grid scheme in which a staggered arrangement of velocity and pressure is adopted, the mass residual can be computed simply by a summation of mass fluxes through primary-cell faces using velocities which are explicitly available at these faces. In contrast, a collocated arrangement necessitates the use of an interpolation method which extracts the face velocities from nodal values.

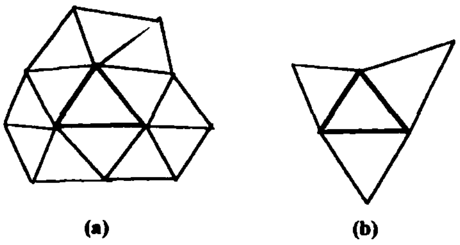
(a) (b)

Figure 6. Numerical stencils associated with pressure-correction equation: (a) equation (24); (b) equation (37)

Linear interpolation might seem an obvious choice, but this practice is incompatible with the Rhie–Chow scheme normally used in a collocated-storage scheme to relate velocity fluctuations at the primary-cell faces to pressure fluctuations at associated neighbouring nodes. Hence the choice of interpolation for determining the cell-face velocities requires considerable care.

In the present semi-staggered strategy, the coupling between pressure and velocity is much stronger than in a fully collocated framework. Occasionally, however, oscillations appear in the pressure field, since the velocity components are stored at a single set of locations.[22,24] To overcome the problem, the Rhie–Chow interpolation scheme was modified for use in the present unstructured method and implemented herein. It is well established that the scheme, when used together with underrelaxation in the momentum equation, can result in converged solutions which depend on the value of the underrelaxation factor. To avoid this dependence, the modifications suggested in References 25–27 were adopted.

For the purpose of explaining how the mass residual is evaluated, it is sufficient to focus attention on one mass flux, say that through the face iv_1–iv_2 of the primary cell in Figure 5. First, upon combining equations (17)–(19), the provisional velocity values at the vertices iv_1 and iv_2 can be expressed as

$$
\begin{aligned}
u^*_{iv_1} &= \alpha\left(H^{u*}_{iv_1} - \frac{1}{2A^u_{iv_1}}\sum_{i=1}^{ie}(p^*_i + p^*_{i+1})(y^c_{i+1} - y^c_i)\right) + (1-\alpha)u^o_{iv_1},\\
u^*_{iv_2} &= \alpha\left(H^{u*}_{iv_2} - \frac{1}{2A^u_{iv_2}}\sum_{i=1}^{ie}(p^*_i + p^*_{i+1})(y^c_{i+1} - y^c_i)\right) + (1-\alpha)u^o_{iv_2},
\end{aligned}
\tag{39}
$$

where, for example,

$$
H^{u*}_{iv_1} = \frac{1}{A^u_{iv_1}}\left(\sum_{i=1}^{ie} A^u_i u^*_{v_i} + \sum_{j=1}^{nb} A^u_{nb} C^u_{nb}(u, v)\right).
\tag{40}
$$

Equations (39) can be rewritten using (29) as

$$
\begin{aligned}
u^*_{iv_1} &= \alpha\left[H^{u*}_{iv_1} - \frac{\Omega_{iv_1}}{A^u_{iv_1}}\overline{\left(\frac{\partial p^*}{\partial x}\right)}_{iv_1}\right] + (1-\alpha)u^o_{iv_1},\\
u^*_{iv_2} &= \alpha\left[H^{u*}_{iv_2} - \frac{\Omega_{iv_2}}{A^u_{iv_2}}\overline{\left(\frac{\partial p^*}{\partial x}\right)}_{iv_2}\right] + (1-\alpha)u^o_{iv_2}.
\end{aligned}
\tag{41}
$$

Oscillations originate from the numerical stencil used for the computation of the pressure derivatives in the momentum equations. The Rhie–Chow interpolation scheme implies the replacement of this pressure derivative (or gradient in the general case) by another expression which enforces the coupling between pressure values on both sides of each edge and the velocity on that edge. To achieve this, face velocities are computed from expressions similar to equation (41):

$$
u^*_e = \alpha\left[H^{u*}_e - \frac{\Omega_e}{A^u_e}\overline{\left(\frac{\partial p^*}{\partial x}\right)}_e\right] + (1-\alpha)u^o_e,
\tag{42}
$$

where now

$$
H^{u*}_e = \tfrac{1}{2}(H^{u*}_{iv_1} + H^{u*}_{iv_2}), \qquad \frac{\Omega_e}{A^u_e} = \frac{1}{2}\left(\frac{\Omega_{iv_1}}{A^u_{iv_1}} + \frac{\Omega_{iv_2}}{A^u_{iv_2}}\right).
\tag{43}
$$

Pressure derivatives on the edge are computed as average values over the auxiliary control volume of Figure 4, using equation (32), in which pressure-correction values should be replaced by pressures.

Substitution of equation (42) and an analogous expression for the provisional v_e-value into equation (38) yields the final value for the mass residual.

Although the mass-flux interpolation scheme, as presented above, is fully incorporated into the present numerical methodology, it has been found that its application is often not necessary as the pressure–velocity coupling seems to be strong enough to prevent oscillations from appearing in the final pressure field. In these cases, cell-edge mass fluxes have been obtained by simple linear interpolation of velocity:

$$u_e^*|_{iv_1-iv_2} = \tfrac{1}{2}(u_{iv_1}^* + u_{iv_2}^*). \tag{44}$$

3.6. *Overall Algorithm*

The whole solution algorithm may be summarized as the following sequence of steps.

1. Initial pressure and velocity fields are defined.
2. The momentum equations (17) and (18) are solved to update the provisional velocity field.
3. The mass imbalance term of equation (37) is computed.
4. The pressure-correction equations (37) are solved.
5. The velocity corrections are obtained from equations (31) using (32), (36a) and (36b).
6. The velocity field is updated using equation (9).
7. The pressure field is obtained using equation (9), with the pressure correction values being underrelaxed prior to the update.
8. Steps 2–7 are repeated until convergence, which is assumed to be reached when the mass residuals in all cells have fallen below a prescribed value.

4. DATA STRUCTURE

One of the key components of any unstructured-grid method is the data structure underlying the method. Any data structure contains mainly connectivity information, i.e. provides the information necessary to connect each grid component (cell, vertex, edge) to adjacent components (not necessarily of the same type). It can also include other types of information, e.g. the 'parent–child' relationship between the geometric elements of an unstructured grid in a dynamically adaptive solution procedure. All the information contributing to a data structure must be stored, and the more information that is stored, the lower tends to be the CPU time consumption associated with recovering unstored data by use of search algorithms. Thus in any unstructured-grid method a compromise has to be struck between memory and CPU time requirements associated with connectivity.

It is recalled that the primary cells of the grid are allowed to be polygons of an arbitrary number of edges and that any integration over a control volume is strictly performed in an anticlockwise direction. Both facts must be accounted for in the data structure that is used in the present algorithm.

For any unstructured grid, connectivity information can be handled within two distinctly different types of data structures. The first is *edge-based* and stores for each edge the identification integers of the two vertices which form the edge and the integers of the two cells which meet on that edge (Figure 7(a)). The second is *cell-based* and stores for each cell the number and identification integers of the edges which form the particular cell (Figure 7(b)). If these two data sets are combined, any geometric information for a 2D unstructured grid can be supplied, irrespective of the shapes of the primary cells of that grid.

Despite the fact that two different storage arrangements appear in the present method, a unified solution approach is achieved. Both the cell-vertex procedure for the momentum equations and the

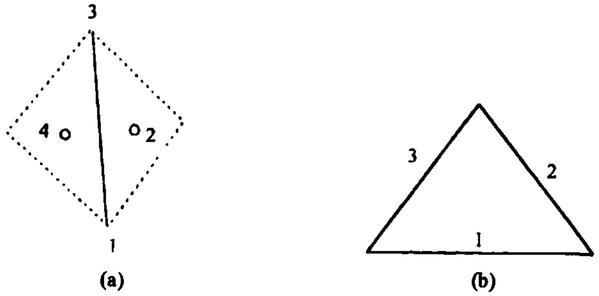

Figure 7. (a) Edge-based and (b) cell-based data structure

cell-centred procedure for the pressure-correction equation are realized by successive sweeps over the edges of the primary cells of the grid. The only difference lies in the fact that an outer loop over the vertices is performed in the former case, while an outer loop over the primary cells is performed in the latter case. The anticlockwise integration over the different control volumes is ensured by the convention implied by Figure 4: for each edge of a primary cell the vertices which form that edge and the cell centres of the two cells adjacent to that edge are stored in contiguous locations in the connectivity matrix. Any reference to the particular edge can then easily reproduce quantities related either to the edge of the primary cell iv_1–iv_2 (Figure 4) and the normal vector $\vec{n}_v$ or to the edge of the macrovolume ic_1–ic_2 and the normal vector $\vec{n}_c$. The one-to-one correspondence between the edges of the primary control volumes and the macrovolumes facilitates code programming and allows handling of different cell shapes in a unified manner. In fact, only minor changes to the actual coding are necessary if the decision is taken to revert from the present semi-staggered approach to a collocated one, whether based on a cell-centred or a cell-vertex arrangement.

5. RESULTS AND DISCUSSION

5.1. Overview

In this section the method presented above is validated by reference to two laminar test cases: the flow in a lid-driven square cavity and the flow over a backward-facing step. In earlier stages of development, inviscid test cases[28] as well as the flow over a flat plate[23] were also considered and successfully computed.

The generation of unstructured grids is not a topic of concern in the present work, nor does it present any challenges in the simple geometries considered below. The simple unstructured (triangular) grids needed here were generated from rectangular meshes by subdividing each quadrilateral cell into four triangles and introducing the appropriate connectivity in accord with the data structure identified in Section 4.

5.2. Lid-driven cavity flow

The lid-driven square cavity flow is a standard benchmark for testing numerical schemes for the NS equations because of its simplicity, the balanced presence of all modes of transport associated with recirculation and the availability of numerous computational solutions in the open literature.

Test calculations have been performed for four values of the Reynolds number: 100, 400, 1000 and 3200. Grid dependence has been investigated for almost all of the cases tested. Furthermore, the sensitivity of the solution to the semi-staggered storage arrangement and the skewness of the grid have been examined in association with alternative momentum-interpolation techniques. A comprehensive presentation and discussion of all test calculations is presented by Thomadakis.[29] Here, only a restricted selection of representative results is included.

In all cases the flow inside the cavity was initially at rest and at constant pressure. No-slip and impermeability conditions were imposed on all walls, with the velocity at the upper wall set equal to unity. A zero-gradient condition was specified along all walls for the pressure correction, which is compatible with a fixed (zero) velocity normal to the walls.

Figure 8 presents the u- and v-velocity profiles along the vertical and horizontal centrelines of the cavity for the case $Re = 100$. Three different grids have been used: a uniform quadrilateral 55 × 55 grid, a 55 × 55 quadrilateral grid clustered towards the walls and a triangular grid which was obtained by subdividing each rectangle of the clustered quadrilateral grid into four triangles (5941 vertices, 11,664 cells). The results obtained are in close agreement with the numerical solutions of Ghia *et al.*[30] and Burggraf.[31] Solutions for $Re = 400$ with the same quadrilateral and triangular grids used for $Re = 100$ are shown in Figure 9. The results obtained with the triangular grid are again in close agreement with the numerical results of Ghia *et al.*, but those obtained with the coarser quadrilateral grid are visibly less accurate.

As the Reynolds number increases, the sensitivity of the solution to the grid density rises markedly. For the highest Reynolds number, $Re = 3200$, a grid-dependence study was initially performed with quadrilateral grids only. The grids chosen included the clustered 55 × 55 mesh used for the $Re = 100$ case and uniform 80 × 80 and 120 × 120 quadrilateral grids, the last mesh being clustered towards the walls. Figure 10 reveals considerable differences between the present 120 × 120 quadrilateral-grid solution and that of Ghia *et al.*, while coarser grids obviously yield even larger discrepancies. In an effort to identify the grid density required to achieve results comparable with those of Ghia *et al.*, the clustered quadrilateral 120 × 120 grid was transformed into a triangular grid by subdividing each rectangle into four triangles. The resulting grid consists of 28,561 vertices and 56,644 cells. The velocity profiles thus obtained and presented in Figure 10 are now seen to be in close agreement with the benchmark data. The outcome of using the same grid for $Re = 1000$ is shown in Figure 11. Here too the computed distributions agree closely with the benchmark data.

One of the major concerns in this study was to identify the influence of the semi-staggered arrangement on the accuracy of the results and on the convergence behaviour. As mentioned earlier, the use of a collocated arrangement results in oscillations in the pressure field due to the poor coupling between pressure and velocity. These oscillations are suppressed when damping is added to the pressure (or pressure-correction) equation, either implicitly, through a special treatment of the

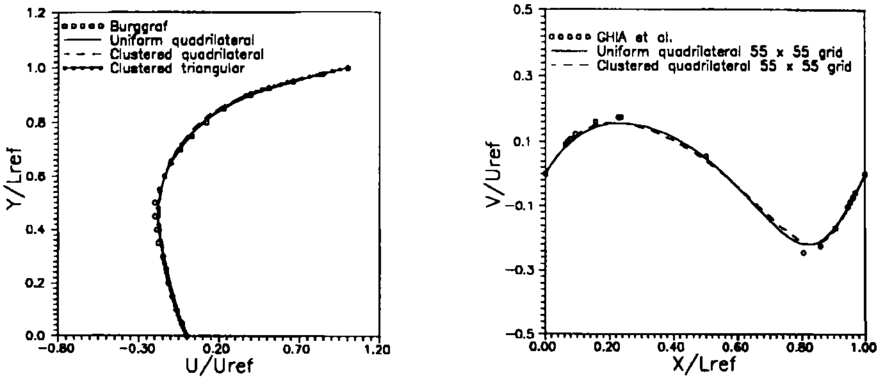

(a) (b)

Figure 8. Cavity flow, $Re = 100$: (a) u-velocity profiles through vertical centreline; (b) v-velocity profiles through horizontal centreline

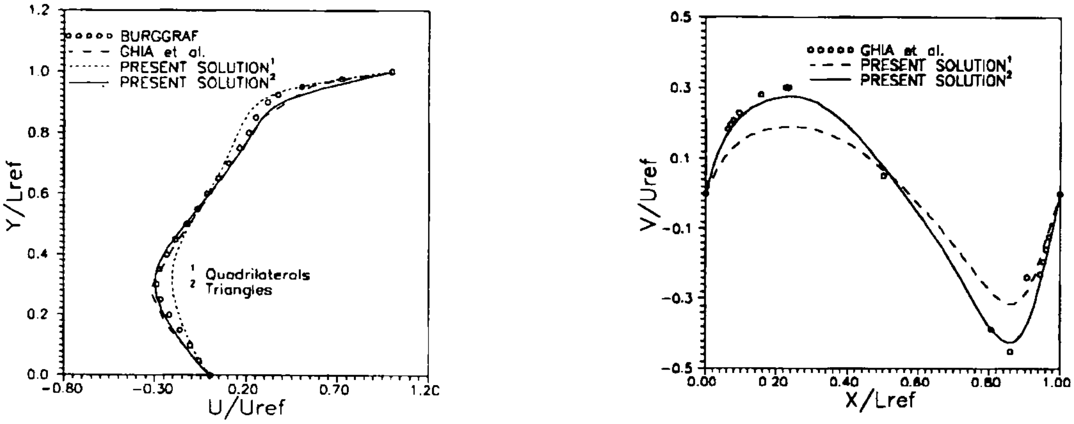

(a)

(b)

Figure 9. Cavity flow, $Re = 400$: (a) u-velocity profiles through vertical centreline; (b) v-velocity profiles through horizontal centreline

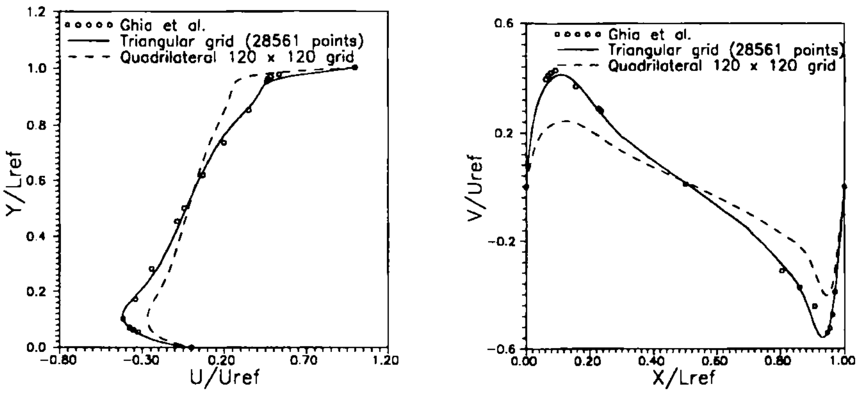

Figure 10. Cavity flow, $Re = 3200$: (left) u-velocity profiles through vertical centreline; (right) v-velocity profiles through horizontal centreline

velocity[20] or pressure terms,[18,19] or explicitly.[17,18] In the present semi-staggered method the pressure field was found to be very smooth, even when no artificial dissipation was added to the solution. Figure 12(a) presents the pressure profiles (expressed in terms $C_p \equiv (p - p_{\text{ref}})/0{\cdot}5\rho U_{\text{lid}}^2$) at various vertical positions along the cavity, for the case of $Re = 3200$, obtained with the 80 × 80 uniform quadrilateral grid. Two sets of curves are presented: one arising from the modified Rhie–Chow interpolation scheme, as described in Section 3.5, and the other obtained without this practice (equation (44)). As is evident from Figure 12(a), the pressure profiles are entirely smooth, even when no artificial dissipation is used, and are virtually indistinguishable. Perfectly smooth results were also obtained for the finer 100 × 100 (not shown) and 120 × 120 quadrilateral grids (Figure 12(b)) as well as for the very fine triangular grid (Figure 12(c)) without the use of the Rhie–Chow interpolation scheme. Results obtained for $Re = 1000$ are entirely consistent with the above observations.

In the present procedure, the angle between any cell face and the line connecting the two cell centres on either side of that face plays an important role in the strength of coupling between pressure and velocity and is thus important to the smoothness of the solution. Figure 13 presents the values of this angle for the finest clustered triangular mesh formed by subdividing the quadrilateral 120 × 120 mesh.

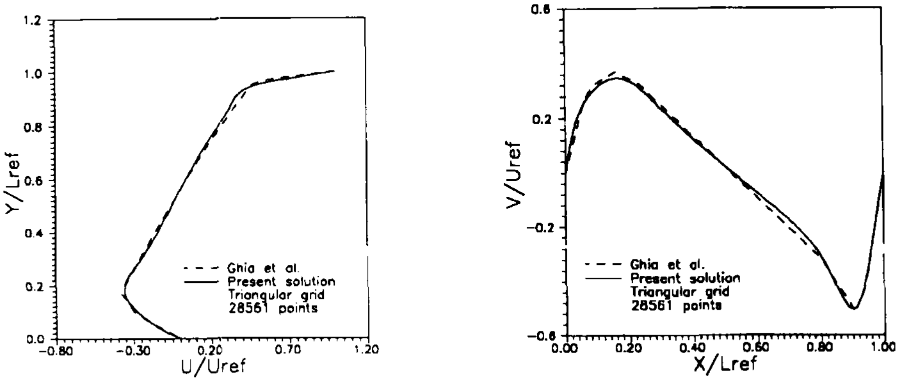

(a) (b)

Figure 11. Cavity flow, $Re = 1000$: (a) u-velocity profiles through vertical centreline; (b) v-velocity profiles through horizontal centreline

The value of this angle, which can be used as a measure of the skewness of the grid, reaches 40° near the boundaries, which represents a high degree of skewness. It is evident therefore that even for a very fine grid, for which the level of artificial diffusion is low, and at a high degree of skewness concurrent with high Reynolds numbers, the present method provides a strong enough coupling between the pressure and velocity fields, thus preventing oscillations.

Some information on the convergence characteristics of the method is finally given in Figure 14. Convergence is characterized by the absolute sum of the mass residuals. The decay of this norm for three values of Re with the quadrilateral uniform 55 × 55 grid is given in Figure 14(a). For $Re = 100$ and 400 the underrelaxation factors for momentum and pressure correction were 0·7 and 0·3 respectively, while values of 0·5 and 0·1 were used for $Re = 3200$. Within any one global iteration, a single inner iteration for momentum and five iterations for pressure correction were executed. Figure 14(b) presents the convergence history for $Re = 3200$ and grids of 80 × 80, 100 × 100 and 120 × 120 quadrilateral cells. The underrelaxation factor for momentum varied between 0·5 and 0·8, while that for pressure correction was held at 0·1. Again, one and five inner iterations per global iteration, were performed for the momentum and the pressure-correction equations respectively. Finally, Figure 14(c) shows the sensitivity of the convergence rate to the number of inner Gauss–Seidel iterations for the pressure-correction equation. The optimum number is seen to be around 20, indicating that satisfaction of mass continuity to a high level of accuracy within any global iteration is a significant contributor to the overall economy of the solution. In all cases a single inner iteration was performed for the momentum equations. Increasing this number did not improve the convergence rate.

5.3. Flow over a backward-facing step

For this second test case, experimental data of Armaly *et al.*[33] are the primary means for assessing the numerical solution. The geometrical details, given in Figure 15, are those of Reference 32, namely upstream channel height $H = 5$ mm, step height $S = 4{\cdot}71$ mm and channel height, aft of the step, $L_{\mathrm{ref}} = 2H$. The Reynolds number, based on L_{ref}, is 389. Two different grids were used: a quadrilateral 80 × 70 grid (5600 vertices, 5451 cells; Figure 16(a)) and the corresponding triangular grid obtained by subdividing each rectangle into four triangles (11,051 vertices, 21,804 cells; Figure 16(b)). Along the inlet boundary the experimental variation in velocity was imposed, while at the outlet the velocities were extrapolated from conditions just upstream of this boundary, in effect representing the imposition of zero-gradient conditions. The computation started from a uniform velocity condition, satisfying

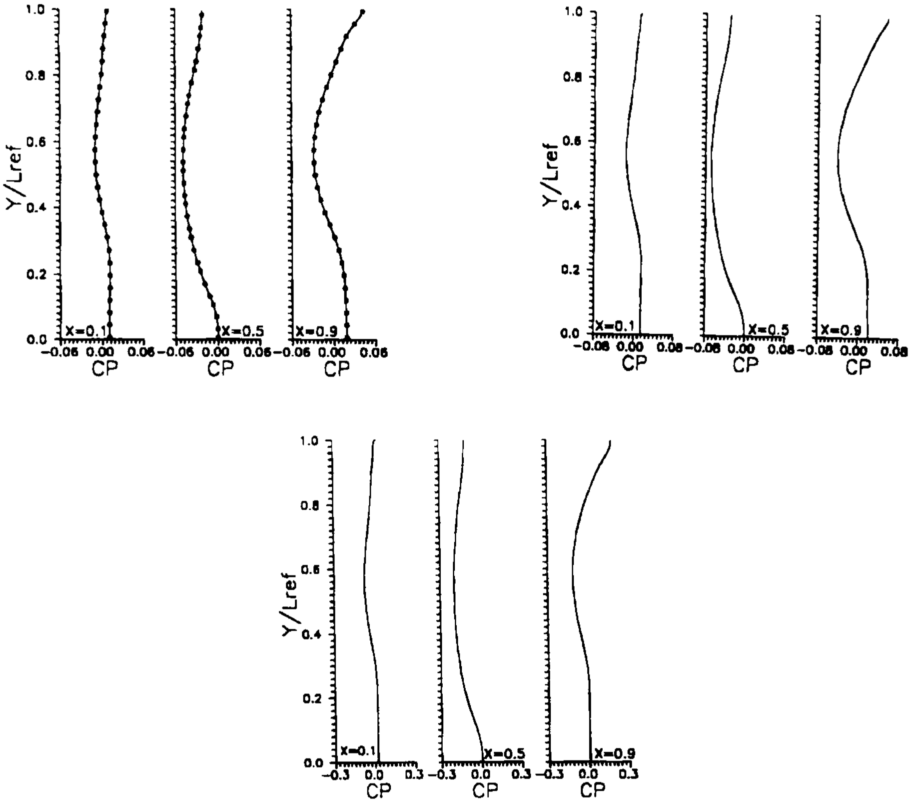

Figure 12. Cavity flow, $Re=3200$: pressure profiles at various x-positions; (top left) uniform 80 × 80 quadrilateral grid: ——— without Rhie & Chow interpolation; • with Rhie & Chow interpolation: (top right) clustered 120 × 120 quadrilateral grid; without Rhie & Chow interpolation; (bottom) fine triangular grid; without Rhie & Chow interpolation

mass continuity. Figure 17 shows a comparison between computed and experimental velocity profiles at various locations along the channel. Agreement is seen to be very close, the solution obtained with the triangular grid being better. The computed reattachment point at $x=3{\cdot}65S$ is very close to the experimental value of $3{\cdot}7S$. With the triangular mesh, approximately 5000 global iterations were required to achieve a reduction of the mass-residual norm by five orders of magnitude.

6. CONCLUSIONS

An unstructured-grid algorithm for incompressible flows has been presented in detail and validated by reference to well-established benchmark data, either numerical or experimental. The key elements of the method can be summarized as follows.

1. Arbitrarily shaped control volumes can be accommodated.
2. The semi-staggered approach implemented provides adequate pressure–velocity coupling in most circumstances.

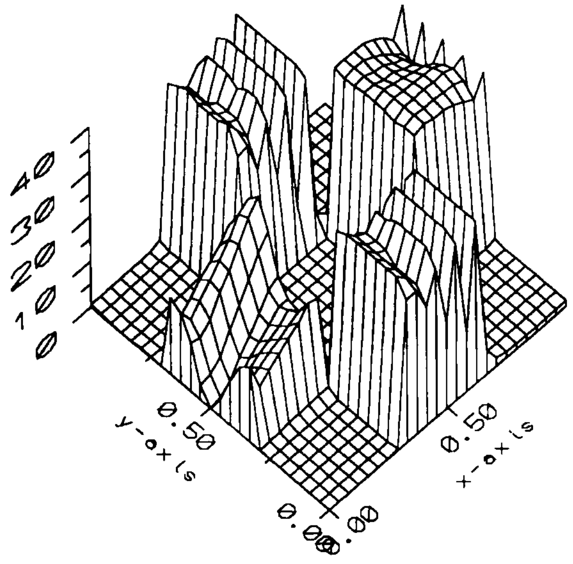

Figure 13. Cavity flow: values of angle between edges and line which connects adjacent cell centres for finest triangular grid

3. In isolated circumstances a further strengthening of the pressure-velocity coupling is advantageous and is effected by a Rhie–Chow type momentum-interpolation technique adapted to the unstructured-grid environment.
4. The improved discretization scheme implemented for the pressure-correction equation provides a stable and robust numerical algorithm.
5. The implementation of a cell-vertex arrangement for the momentum equations and a cell-centred arrangement for the pressure-correction equation is successfully handled by the edge-based data

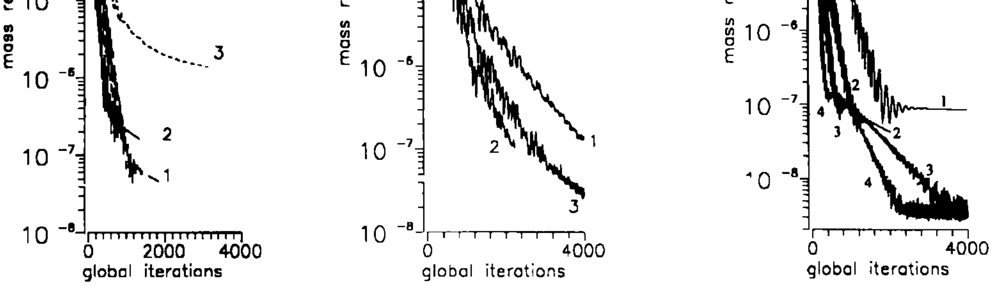

(a) (b) (c)

Figure 14. Cavity flow: convergence histories for various test cases (n_p, number of internal iterations for pressure-correction equation; n_u, corresponding number of iterations for momentum equations)

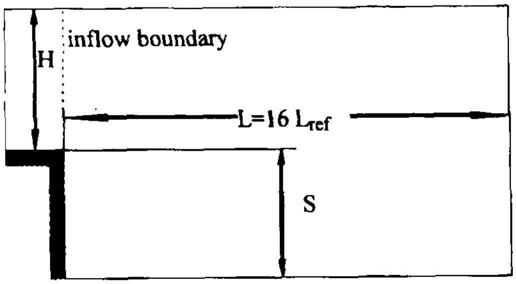

Figure 15. Backward-facing step flow: geometry

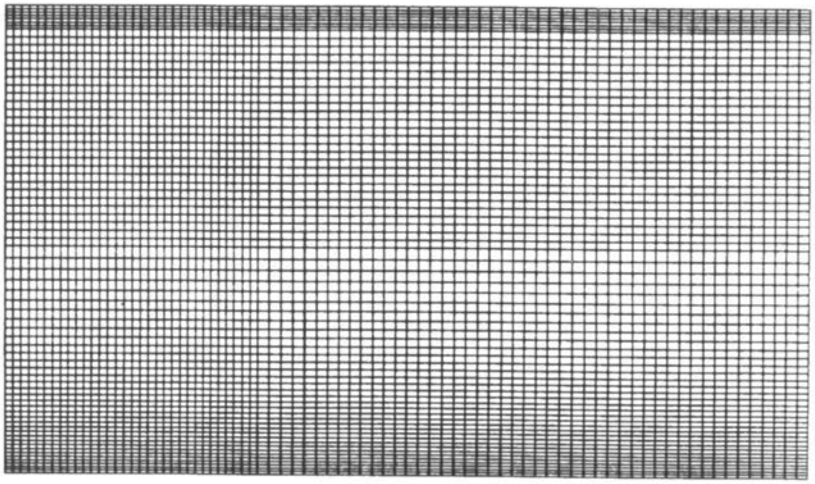

(a)

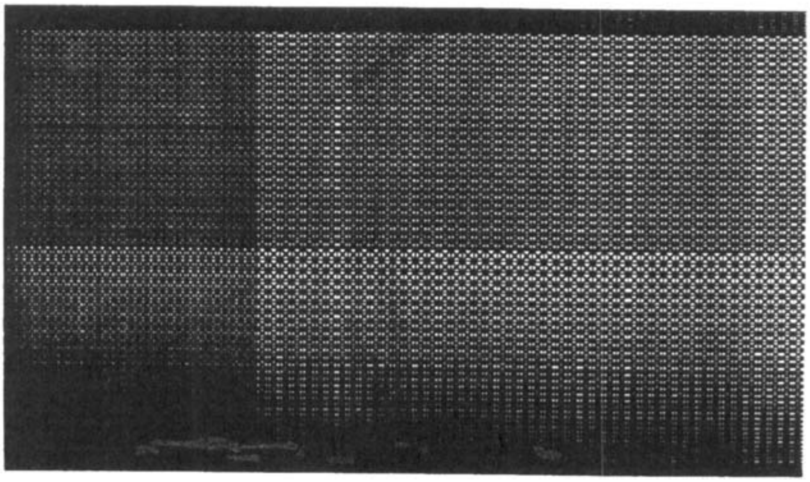

(b)

Figure 16. Backward-facing step flow: (a) quadrilateral 80 × 70 grid; (b) triangular grid

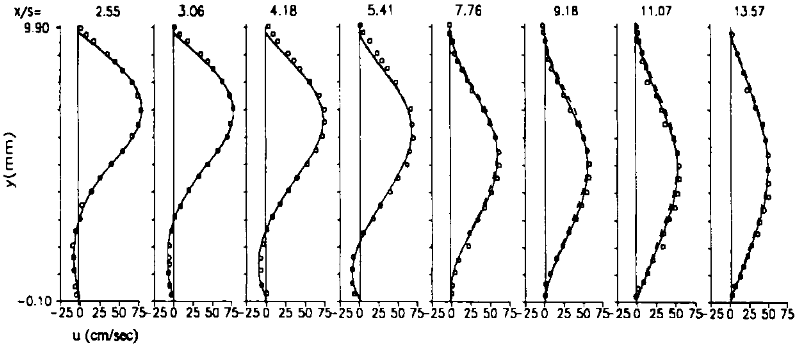

Figure 17. Backward-facing step flow: velocity profiles (- - -, quadrilateral 80 × 70 grid; ——, triangular grid; o, experimental data[33])

structure. Despite the conceptual complexity that this arrangement imposes, the actual coding of the method is quite straightforward and simple.

6. Higher-order convection approximations are necessary to improve the numerical accuracy and hence to reduce grid-density requirements; this aspect is now being pursued, as is a more implicit solution scheme designed to reduced the number of iterations required to achieve convergence.

ACKNOWLEDGEMENTS

This work was supported by a grant awarded to the first author by the Commission of the European Communities under the Human Capital and Mobility Programme (Project ERB4001GT921959). This support is gratefully acknowledged.

REFERENCES

1. B. R. Baliga and S. V. Pataknar, 'A new finite-element formulation for convection–diffusion problems', *Numer. Heat Transfer*, **3**, 393–409 (1980).
2. B. R. Baliga and S. V. Pataknar, 'A control volume finite-element method for two-dimensional fluid flow and heat transfer', *Numer. Heat Transfer*, **6**, 245–261 (1983).
3. B. R. Baliga, T. T. Pham and S. V. Patankar, 'Solution of some two-dimensional incompressible fluid flow and heat transfer problems, using a control volume finite-element method', *Numer. Heat Transfer*, **6**, 263–282 (1983).
4. S. Ramadhyani and S. V. Patankar, 'Solution of the convection–diffusion equation by a finite-element method using quadrilateral elements', *Numer. Heat Transfer*, **8**, 595–612 (1985).
5. C. Prakash, 'An improved control volume finite-element method for heat and mass transfer, and fluid flow using equal-order velocity–pressure interpolation', *Numer. Heat Transfer*, **9**, 253–276 (1996).
6. C. Prakash, 'Examination of the upwind (donor-cell) formulation in control volume finite-element methods for fluid flow and heat transfer', *Numer. Heat Transfer*, **11**, 401–416 (1987).
7. C. Prakash and S. V. Patankar, 'A control-volume finite-element method for predicting flow and heat transfer in ducts of arbitrary cross-sections—Part I: Description of the method', *Numer. Heat Transfer*, **12**, 389–412 (1987).
8. C. Prakash and S. V. Patankar, 'A control-volume finite-element method for predicting flow and heat transfer in ducts of arbitrary cross-sections—Part II: Application to some test problems', *Numer. Heat Transfer*, **12**, 413–437 (1987).
9. B. LeDain Muir and B. R. Baliga, 'Solution of 3D convection–diffusion problems using tetrahedral elements and flow-oriented upwind interpolation function', *Numer. Heat Transfer*, **9**, 143–162 (1986).
10. N. A. Hookey, B. R. Baliga and C. Prakash, 'Evaluation and enhancements of some control volume finite element methods—Part 1: Convection–diffusion problems', *Numer. Heat Transfer*, **14**, 255–272 (1988).
11. N. A. Hookey, B. R. Baliga and C. Prakash, 'Evaluation and enhancements of some control volume finite element methods—Part 2: Incompressible fluid flow problems', *Numer. Heat Transfer*, **14**, 273–293 (1988).
12. C. Masson, H. J. Saabas and B. R. Baliga, 'Co-located equal-order control-volume finite element method for 2D axisymmetric incompressible fluid flow', *Numer. Heat Transfer*, **18**, 1–26 (1994).
13. R. D. Lonsdale and R. Webster, 'The application of finite volume methods for modelling 3D incompressible flow on an unstructured mesh', *Proc. 6th Int. Conf. on Numerical Methods in Laminar and Turbulent Flow*, Pineridge, Swansea, 1989, pp. 1615–1625.

14. G. K. Despotis and S. Tsangaris, 'A fractional step method for the solution of incompressible Navier–Stokes equations on unstructured triangular meshes', *Int. j. numer. methods fluids*, **20**, 1273–1288 (1995).
15. A. J. Chorin, 'A numerical method for solving incompressible viscous flow problems', *J. Comput. Phys.*, **2**, 12–21 (1967).
16. M. Williams, 'The solution of the 2D incompressible flow equations in unstructured triangular meshes', *Numer. Heat Transfer*, **23**, 309–325 (1993).
17. J. K. Watterson, 'A pressure-based flow solver for the 3D Navier–Stokes equations on unstructured and adaptive meshes', *AIAA Paper 94-2358*, 1994.
18. A. Gosman, C. Kralj, C. Marooney and P. Theodossopoulos, 'Development strategies for diesel combustion simulation using the SPEED code', *I.Mech.E.* paper *C448/035*, 1992
19. M. J. Raw, P. F. Galpin, B. R. Hutchinson, G. D. Raithby and J. P. Van Doormaal, 'An element-based finite-volume method for computing viscous flows', Internal Report, *Advanced Scientific Computing Inc.*, 1994.
20. C. M. Rhie and W. L. Chow, 'Numerical study of the turbulent flow past an airfoil with trailing edge separation', *AIAA J.*, **21**, 1525–1532 (1983).
21. S. P. Vanka, 'Block implicit multigrid solution of Navier–Stokes equations in primitive variables', *J. Comput. Phys.*, **65**, 138–158 (1986).
22. S. V. Patankar and D. B. Spalding, 'A calculation procedure for heat, mass and momentum transfer in 3D parabolic flows', *Int. J. Heat Mass Transfer.*, **15**, 1787 (1972).
23. M. P. Thomadakis and M. A. Leschziner, 'Numerical solution of viscous incompressible flows using a pressure-correction method and unstructured grids', in S. Wagner *et al.* (eds), *Proc. 2nd Eur. CFD Conf.*, Wiley, 1994, pp. 325–332.
24. H. Iacovides, private communication, UMIST, 1994.
25. T. F. Miller and F. W. Schmidt, 'Use of a pressure-weighted interpolation method for the solution of the incompressible Navier–Stokes equations on a nonstaggered grid system', *Numer. Heat Transfer*, **14**, 213–233 (1999).
26. S. Majumdar, 'Role of underrelaxation in momentum interpolation for calculation of flow with nonstaggered grids', *Numer. Heat Transfer*, **13**, 125–132 (1988).
27. F. S. Lien 'Computation and modelling of 3D flows in complex ducts and passages', *Ph.D. Thesis*, UMIST, 1992.
28. M. P. Thomadakis and M. A. Leschziner, 'An unstructured-grid algorithm for incompressible flow', *Proc. 6th Bienn. Colloq. on CFD*, UMIST, Manchester, 2.3–2.4, May 1994.
29. M. P. Thomadakis, 'Development and validation of computer-based procedure for simulating turbulent engineering flows with unstructured numerical grids and transport models of turbulence', *UMIST Internal Rep.*, FLAIR/CEC 94-2, 1994.
30. U. Ghia, K. N. Ghia and C. T. Shin, 'High Resolutions for incompressible flow using the Navier–Stokes equations and a multigrid method', *J. Comput. Phys.*, **48**, 387–411 (1982).
31. O. R. Burggraf, 'Analytical and numerical studies of the structure of steady separated flow', *J. Fluid Mech.*, **24**, 113–115 (1966).
32. B. F. Armaly, F. Durst, J. C. F. Pereira and B. Schoenung, B. 'Experimental and theoretical investigation of backward-facing step flow', *J. Fluid Mech.*, **127**, 473–496 (1983).